Comparing Sensitivities of Geodetic Processing Methods for Rapid Earthquake Magnitude Estimation

Tim Dittmann*[1], Kathleen Hodgkinson[1,2], Jade Morton[3], David Mencin[1], and Glen S. Mattioli[1]

Abstract

Rapid earthquake magnitude estimation from real-time space-based geodetic observation streams provides an opportunity to mitigate the impact of large and potentially damaging earthquakes by issuing low-latency warnings prior to any significant and destructive shaking. Geodetic contributions to earthquake characterization and rapid magnitude estimation have evolved in the last 20 yr, from post-processed seismic waveforms to, more recently, improved capacity of regional geodetic networks enabled real-time Global Navigation Satellite System seismology using precise point positioning (PPP) displacement estimates. In addition, empirical scaling laws relating earthquake magnitude to peak ground displacement (PGD) at a given hypocentral distance have proven effective in rapid earthquake magnitude estimation, with an emphasis on performance in earthquakes larger than $\sim M_w$ 6.5 in which near-field seismometers generally saturate. Although the primary geodetic contributions to date in earthquake early warning have focused on the use of 3D position estimates and displacements, concurrent efforts in time-differenced carrier phase (TDCP)-derived velocity estimates also have demonstrated that this methodology has utility, including similarly derived empirical scaling relationships. This study builds upon previous efforts in quantifying the ambient noise of three-component ground-displacement and ground-velocity estimates. We relate these noise thresholds to expected signals based on published scaling laws. Finally, we compare the performance of PPP-derived PGD to TDCP-derived peak ground velocity (PGV), given several rich event datasets. Our results indicate that TDCP-PGV is more likely than PPP-PGD to detect intermediate magnitude ($\sim M_w$ 5.0–6.0) earthquakes, albeit with greater magnitude estimate uncertainty and across smaller epicentral distances. We conclude that the computationally lightweight TDCP-derived PGV magnitude estimation is complementary to PPP-derived PGD magnitude estimates, which could be produced at the network edge at high rates and with increased sensitivity to ground motion than current PPP estimates.

Cite this article as Dittmann, T., K. Hodgkinson, J. Morton, D. Mencin, and G. S. Mattioli (2022). Comparing Sensitivities of Geodetic Processing Methods for Rapid Earthquake Magnitude Estimation, *Seismol. Res. Lett.* **93**, 1497–1509, doi: 10.1785/0220210265.

Introduction

Global Navigation Satellite System (GNSS) processing

The GNSS consists of multiple medium-earth-orbit satellite constellations broadcasting precise timing L-band multifrequency signals toward Earth. A GNSS receiver and antenna combination amplifies and demodulates these incoming low-power signals to continuously track the broadcast signal, and convert it to range and carrier phase measurements. These phase measurements are highly precise but contain unknown integer biases. Precise point positioning (PPP) (Zumberge *et al.*, 1997) with ambiguity resolution, also known as PPP-AR (Bertiger *et al.*, 2010), is a position estimation method in which these carrier phase biases are estimated to achieve uncertainties of several centimeters in horizontal antenna positions. Many approaches exist to accomplish this level of precision, but most depend on reducing uncertainties through precise satellite clock error estimates, precise satellite orbit determination estimates, and multifrequency carrier-phase data to remove first-order ionospheric effects. This study uses PPP estimated in real

1. UNAVCO, Inc., Boulder, Colorado, U.S.A., https://orcid.org/0000-0002-6104-7190 (TD); https://orcid.org/0000-0001-8529-0913 (KH); https://orcid.org/0000-0001-9984-6724 (DM); 2. Now at Sandia National Laboratories, Albuquerque, New Mexico, U.S.A.; 3. Ann and H. J. Smead Aerospace Engineering Sciences Department, University of Colorado Boulder, Boulder, Colorado, U.S.A., https://orcid.org/0000-0001-9173-2888 (JM)

*Corresponding author: dittmann@unavco.org

time by the Trimble RTX (Leandro *et al.*, 2011) software. These positions are estimated once per second from 1 Hz GNSS observations streamed from the remote receiver to a central network operations center (NOC) and are typically available with 1–2 s latency, in which latency is defined as the time difference between observations encoded at the receiver and availability from the data center (Murray *et al.*, 2019). The low latencies for the real-time PPP solutions from the GNSS component of the Network of the Americas (NOTA) make them useful to safety of life and hazard applications (Mattioli *et al.*, 2020). Once at the NOC, positions are computed in a geodetic reference frame and translated to a topocentric reference frame as relative displacements from an a priori position. The RTX software is a commercial product using proprietary positioning software and data products, including the satellite orbits and clocks, and it has proven capable of tracking medium-to-large (M_w 6.0+) seismic displacements (Hodgkinson *et al.*, 2020).

A partially independent geodetic processing method using the same "raw" GNSS observations is known as the time-differenced carrier phase (TDCP) method (van Graas and Soloviev, 2004) and was first proposed for capturing seismic waveforms by Colosimo *et al.* (2011). This processing method estimates antenna velocity by differencing the phase observations between two epochs, instead of solving for the unknown integer ambiguity at each epoch. This change in phase over time is equivalent to the pseudorange rate or Doppler shift. By assuming no change in carrier phase integer ambiguity nor substantial epochwise dynamic atmospheric change, the integer ambiguity and atmospheric effects are effectively removed. For a complete description of this method, see Colosimo *et al.* (2011), Misra and Enge (2011), Grapenthin *et al.* (2018), and Crowell (2021).

The novel Variometric Approach for Displacements Analysis Standalone Engine method (Colosimo *et al.*, 2011) integrates these velocities over time to estimate displacements. In our study, we complete our analysis in velocity space using the open-source SNIVEL package (see Data and Resources). The SNIVEL software uses the narrow lane, Global Positioning System (GPS)-only, dual-frequency phase combination, and currently does not account for tides, higher order ionospheric effects, atmospheric gradients, or cycle slips, which are partially addressed in the following. Without the need for sophisticated corrections or additional earth models for real-time processing, a major advantage of the TDCP processing method is that it can be pushed to the network edge in real time with a relatively low computational and financial cost.

Peak geodetic signals for rapid magnitude estimation

The ability for high rate GNSS to track coseismic and dynamic displacements is well established (Larson *et al.*, 2003; Genrich and Bock, 2006), and advances in network design, coupled with improved real-time processing, have enabled relatively precise estimates of these waveforms in real time and furthering their utility for hazards applications (Allen and Ziv, 2011). Crowell *et al.* (2013), Melgar *et al.* (2015), and Ruhl *et al.* (2019) have demonstrated the usefulness of the empirical relationship between peak ground displacement (PGD) estimated from higher rate, unsaturated PPP displacements, earthquake magnitude, and distance from the seismic source using scaling law coefficients of log-linear regression models from catalogs of recent earthquakes. In addition, these higher rate estimates enable geodetic infrastructure to act as a strong-motion instrument (Larson, 2009; Crowell, 2021), and complement existing accelerometer and seismometer early warning infrastructure.

Fang *et al.* (2020) developed a similar log-linear regression model relating earthquake magnitude, hypocentral distance, and peak ground velocity (PGV) estimated from TDCP velocities using a catalog of recorded recent earthquakes. The GNSS TDCP-derived velocities can be sensitive to compressional (*P*) waves (Hohensinn and Geiger, 2018) and show good agreement with U.S. Geological Survey (USGS) ShakeMap velocities (Grapenthin *et al.*, 2018; Crowell, 2021), further enhancing the value of this processing method for hazards research and real-time assessments by complementing existing seismic infrastructure, and potentially filling geographic or temporal availability gaps. Here, we present a noise model of the three-component displacements and velocities, and compare these with the expected coseismic signals based upon the existing empirical scaling laws. We then select a threshold to quantify and compare the probability of false alerts and probabilities of detection across the processing methods. In addition, we investigate possible station-dependent sources of noise correlated with station attributes. Finally, we compare these expected signals and noise with results from two actual events of different magnitudes.

Methods

Dataset

This study establishes a noise assessment of PPP-PGD and TDCP-PGV using a dataset of concurrent 1 Hz Trimble RTX PPP estimates and 1 Hz GPS raw observations at 592 stations distributed across North America from 16:00–17:00 UTC on 4 July 2019. The 2019 Ridgecrest earthquake sequence initiated at 17:50 UTC on this day with an M_w 6.4 event. Larger seismic events (M_w >6.0) within the NOTA footprint initiate a data response to recover complete high-rate data files (Mattioli *et al.*, 2020). The time interval for this study was selected because of the availability of complete higher rate data due to the earthquake-initiated data response during a period of no known external dynamic signals. There is no prior seismic activity in the time window greater than M_w 3.0 (as published by the Advanced National Seismic System [ANSS] Comprehensive Catalog of Earthquake Events and Products) within the NOTA footprint. In addition, space weather indices

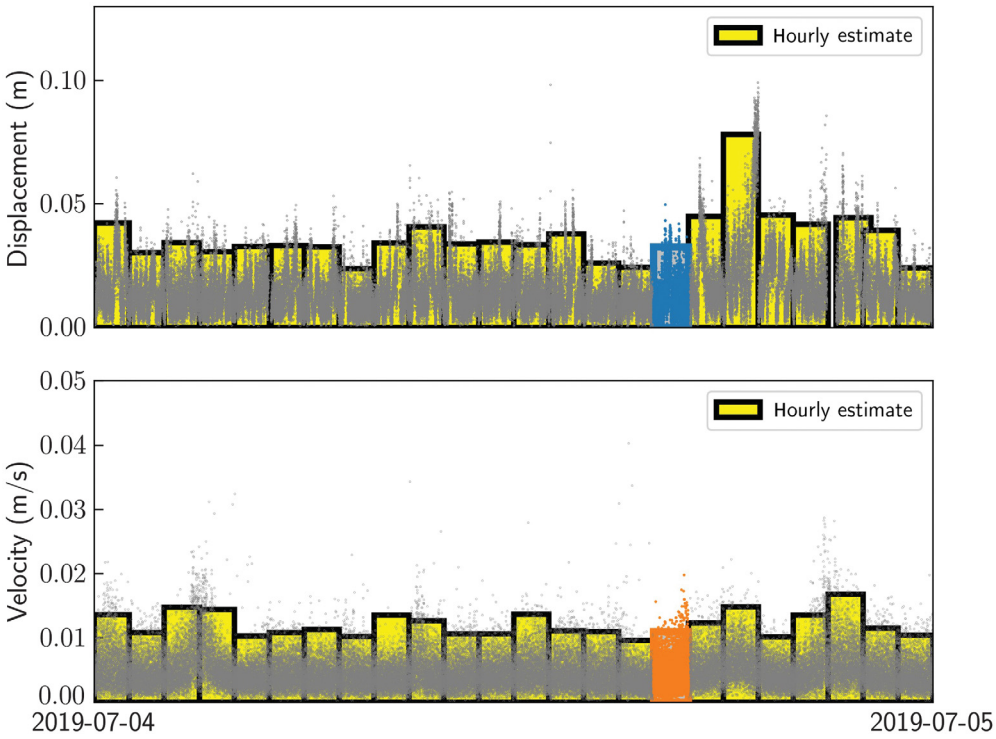

Figure 1. Twenty-four hour evaluation of variance of 1 hr noise estimates for station P509 over 24 hr. The black dots are the 1 Hz precise point positioning (PPP) displacement and time-differenced carrier phase (TDCP) velocity estimates derived from the three-component waveforms. The yellow bars are the hourly noise estimates based upon a 99.5% confidence level upper threshold given an NCX2 distribution. The blue bar and orange bar are the displacement and velocity estimates, respectively, used in the temporal window of this study.

indicate calm space weather conditions, with the daily Ap index reported at 4 nT (see Data and Resources), which implies a low ionospheric gradient at the NOTA primarily mid-latitude stations. We infer that the completeness of the NOTA dataset combined with the atmospheric and tectonic stability of the temporal epoch makes it optimal for 1 Hz ambient noise characterization. This study investigated different variance estimation periods by examining 24 hr of data from station P509 (Fig. 1) and conclude that 1 hr was a reasonable window for the characterization of our noise estimates.

The ambient noise of the 1 Hz position displacement estimates is dependent on many factors, including the performance of the positioning algorithm, the GNSS constellations tracked and included in the processing, multipath noise, unmodeled atmospheric conditions, and local radio interference. Our PPP noise characterization assumes the same positioning algorithm, and no physical displacement dynamics occur in the window of characterization, such that any relative variance in station-dependent PPP noise is assumed to be a function of raw observation quality including multipath, antenna or receiver performance, differences in signals tracked, and any unlikely but possible systematic station bias in corrections model errors. This assessment mitigates the latter impact by consistent windowing in time and space. Typical noise values are at the centimeter level. Previous studies have demonstrated the value of using only horizontal displacements in earthquake magnitude inversions to minimize the impact of the noisier vertical position estimates (Melgar *et al.*, 2019). For consistency, however, we use the 3D scaling laws, which might prove invaluable for an event with significant vertical signals such as those expected from great earthquakes generated on the subduction interface. Ambient noise in TDCP velocity estimates is directly related to receiver carrier phase noise. Receiver manufacturers are able to minimize phase noise using higher quality oscillators and advanced carrier phase tracking loop filtering, including radio frequency interference or signal multipath mitigation. Typical noise values are around a centimeter per second.

Establishing a robust three-component noise threshold

By estimating a station-dependent, ambient noise threshold, Hodgkinson *et al.* (2020) established NOTA real-time GNSS sensitivity to published PGD scaling law magnitude detection for earthquakes that occur within its spatial footprint. Each contributing station's three-component magnitude time-series threshold was derived from a heuristic statistic of the time-series median plus three times the time-series median absolute deviation over a specified period. This station threshold was then used to represent the noise floor of the three-component magnitude above which the signals of interest, peak displacement waveforms, can be detected at any NOTA real-time station. Peaks below the established station-specific threshold are considered noise and thus not included in any scaling law magnitude inversion estimate. Nonseismic peak ground motions above the threshold are considered false positives (FPs). We build upon the previous noise threshold approach established by Hodgkinson *et al.* (2020) by more accurately representing the sampling distribution model as follows.

We observe Trimble RTX position time-series topocentric displacements, δ_{north}, δ_{east}, δ_{up} and TDCP velocity components, vel_{north}, vel_{east}, vel_{up}, are normally distributed variables

TABLE 1
Probability of False Positive (FP) Rate Observed Over 24 Hr, in Which FP is the Percentage of FPs Out of the Total Number of Epochs in the Test Window

Station	Method	Hodgkinson *et al.* (2020) FP	99.95 NCX2 FP	99.99 NCX2 FP
P509	PPP-GD	2.6%	1.4%	0.5%
	TDCP-GV	2.8%	0.5%	0.2%
CLGO*	PPP-GD	2.7%	1.4%	0.5%
	TDCP-GV	3.5%	1.8%	0.9%
SC00	PPP-GD	3.0%	1.6%	0.7%
	TDCP-GV	3.0%	1.4%	0.6%
P041	PPP-GD	2.8%	1.5%	0.5%
	TDCP-GV	3.5%	1.9%	1.3%

PPP-GD, precise point positioning-derived ground displacement; TDCP-GV, time-differenced carrier phase-derived ground velocity.
These data are processed using an identical approach to the network estimates of 15 min windows with a coarse nongeophysical outlier removal, described in detail in the next section. Hodgkinson *et al.* (2020) selects a threshold, given the median value plus three times the mean absolute deviation; the rightmost 2 columns use different α values in the NCX2 best-fit distributions.
*CLGO was tested over a 22 hr arc.

with respective nonzero means, μ_{north}, μ_{east}, μ_{up}. The ground displacement (GD) and ground velocity (GV) are related to the sum of the squares of the normally distributed components:

$$\text{GD} = \sqrt{\delta^2_{\text{east}} + \delta^2_{\text{north}} + \delta^2_{\text{up}}}, \tag{1}$$

$$\text{and} \quad \text{GV} = \sqrt{\text{vel}^2_{\text{east}} + \text{vel}^2_{\text{north}} + \text{vel}^2_{\text{up}}}. \tag{2}$$

A random variable representing the sum of the squares of normally distributed, independent random variables can be approximated by the noncentral chi-squared distribution (NCX2) (Sheldon James Press, 1966), defined by k degrees of freedom equal to three and noncentrality parameter, lambda, equal to the sum of the square of the means of each component:

$$\lambda = \sum_{n=1}^{3} \mu_i^2. \tag{3}$$

We observe that the distribution of the sum of the squares of the components can be approximated by a chi-squared distribution. The aforementioned k and estimated λ values seed the Scipy scientific package for fitting a maximum-likelihood estimate (see Data and Resources) of the scale and location of a distribution that fits each station's hour-long time-series square of components summation. This allows us to characterize each station's ambient noise by using the fitted noncentral chi-squared probability distribution function (PDF):

$$f(x, k, \lambda) = \frac{1}{2}\left(e^{-\frac{(\lambda+x)}{2}}\right)(x/\lambda)^{\frac{k-2}{4}} I_{(k-2)/2}(\sqrt{\lambda x}), \tag{4}$$

in which $I_{k-2/2}$ denotes the modified Bessel function of order $(k-2)/2$ (see Data and Resources: Scipy package).

We acknowledge that PPP displacements and TDCP velocities are not independent measurements, and thus this distribution is mathematically inaccurate. Empirically we find that this distribution offers a more meaningful noise model over the previous heuristic threshold metric of Hodgkinson *et al.* (2020). Future work into applying a more sophisticated model, such as a parameterized gamma distribution (Ferrari, 2019), could improve accuracy.

The NCX2 PDF of the three-component squared summation enables a significance quantile, α, to be used as a threshold to balance the probability of detection, PD (or true positive), with a probability of FP or false alert (PFA), in which PFA is $\approx 1-\alpha$. Observed FP rates exceed anticipated sample significance quantiles in Table 1; this is possibly a result of correlated noise that is not accounted for in this distribution. Figure 2 illustrates our detection sensitivity balance: increasing α shifts the vertical, red dashed line to the right, which has the effect of decreasing PFA (gray area in panels a and b), while increasing the probability of a missed detection or false negative (gray area in the panels c and d). These expected signals are based upon the normally distributed empirical scaling laws, using the coefficients of Melgar *et al.* (2015) and Fang *et al.* (2020). Table 1 quantifies these false alert rates, with α as a tunable parameter for the decision balance in such a system. We consider our selection of the quantile threshold further in the next section.

Determining an optimal noise threshold

We evaluate a range of probabilities of the best-fit NCX2 distribution to explore the relationship between PFA and PD (Fig. 3), given a median noise model across the 592 stations. Assessing societal false-alert tolerance in combination with human and infrastructure costs of missed earthquake early warning (EEW) is outside the scope of this work. We recognize an operational early warning system, however, would require a rigorous analysis for this impactful parameter selection (Minson *et al.*, 2019). In this study, we select the 99.5% quantile for our methodology comparison. At any quantile level chosen, individual station false alerts within an operational EEW system could be mitigated by correlating with spatially adjacent GNSS and seismic equipment. The thresholds are applied consistently across both the processing methods for this relative evaluation.

Our study uses the displacement scaling coefficients of Melgar *et al.* (2015) for modeling the expected displacement signal at a given hypocentral distance and magnitude. This expected signal is then related to the station-dependent estimated displacement

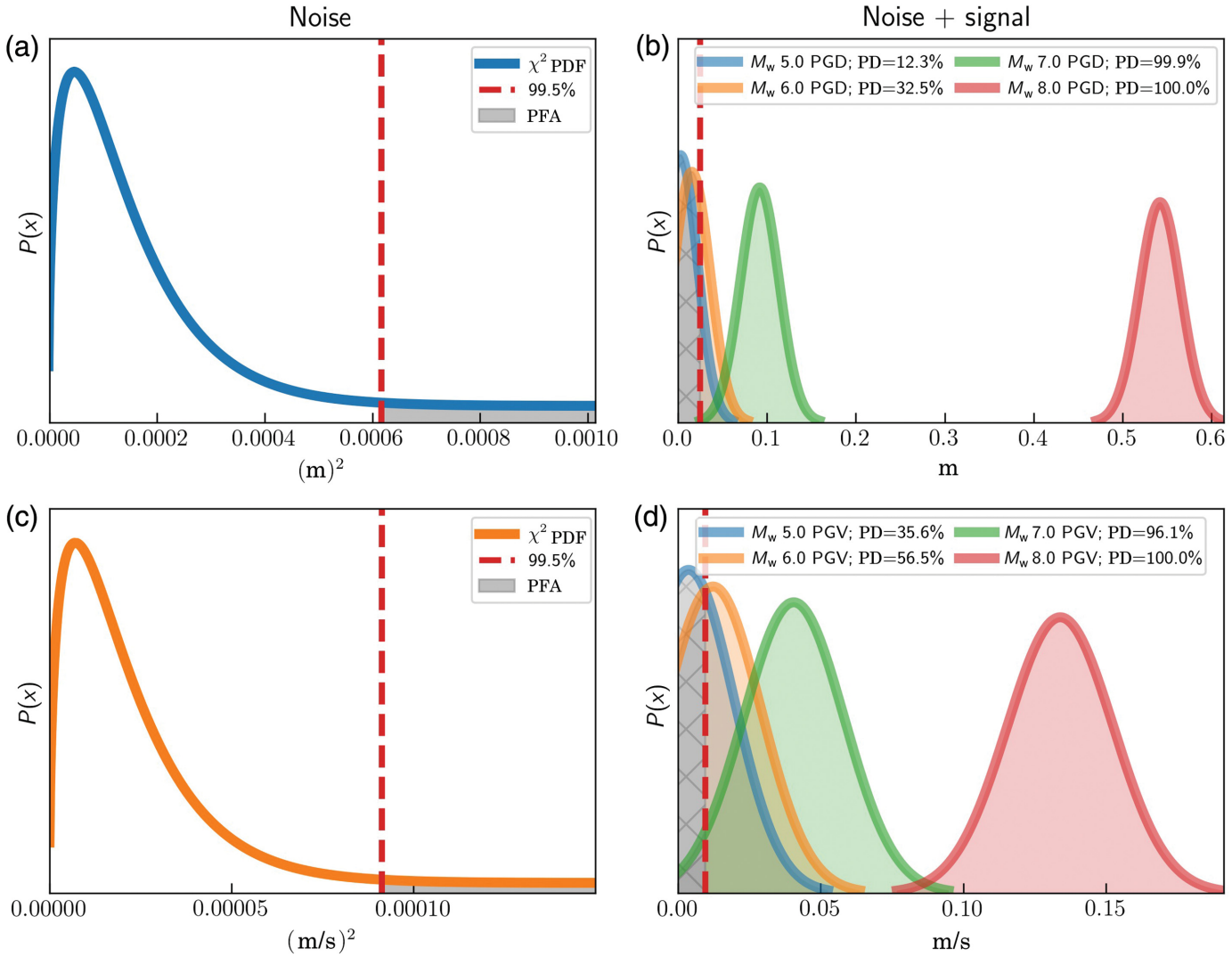

Figure 2. Panels (a) and (c) are the displacement and velocity NCX2 noise models (panel a: PPP-derived peak ground displacement [PGD]; panel b: TDCP-derived peak ground velocity [PGV]) for an example station (P509) with the selected threshold of a 99.5% significance interval. The region of false alert is shaded in gray (PFA). Panels (b) and (d) are the probability distribution functions of a range of different magnitude events given normally distributed expected (b) PGD and (d) PGV signals and variances of the Melgar *et al.* (2015) and Fang *et al.* (2020) scaling laws at a fixed hypocentral distance of 100 km. The selected thresholds are mapped to displacement and velocity spaces to capture probability of detection (PD) for these events. Panels (b) and (d) illustrate TCDP velocity has higher PD for the medium events (M_w 5.0 and 6.0). They also indicate the larger magnitude events (M_w 8.0) gain signal at a higher rate in displacement space, evident with the relative spacing between the threshold and the expected signals.

noise, the result of which we consider the sensitivity to an earthquake, given its distance and magnitude. We used a windowing method similar to that of Hodgkinson *et al.* (2020) to evaluate the ambient noise: for each site, a 1 hr window is divided into 15 min segments, in which the median displacement of the first 300 s is used as the reference for the entire window. This reduces the effect of longer period drift present in RT-GNSS PPP solutions and is more comparable to a moving window process that would be implemented in real-time monitoring. This approach has an effect similar to removing the long-term average used by traditional seismic event pickers, such as the one applied to GNSS data by Ohta *et al.* (2012). We find fitting a distribution to the sample data is sporadically affected by large outliers; accordingly, we do a simple threshold mask and remove any nongeophysical single epoch offsets greater than 2 m, which could easily be implemented in real time. The station-dependent noise threshold is set as the 99.5% significance of the noncentral chi-squared distribution fit to the quiescent 1 hr time window of each site.

For TDCP-PGV-derived magnitude estimates and sensitivity, this study uses the velocity scaling coefficients of Fang *et al.* (2020) to model the expected TDCP velocity signals at a given hypocentral distance and earthquake magnitude. In our TDCP processing method, cycle slip impacts are limited to individual epoch differences, but they are not detected in this current

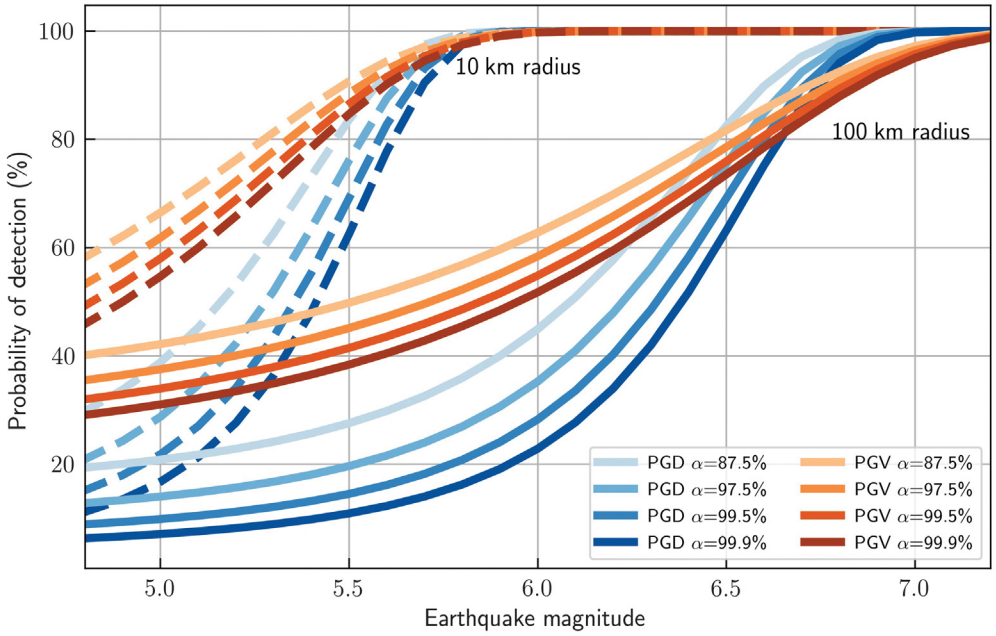

Figure 3. Probability of detection as a function of earthquake magnitude over a range of α values fixed hypocentral distances of 10 and 100 km, in which α is the quantile used within a best-fit NCX2 distribution. We use the 592-station median threshold at each quantile for the basis of the noise distribution, and the scaling laws of Melgar *et al.* (2015) and Fang *et al.* (2020) as the basis for the expected signal plus noise. It is worth noting that this illustration does not account for accuracy of detection.

SNIVEL implementation. We currently minimize the impact of cycle slips and other possible nongeophysical outliers using a coarse threshold set to 1 m/s, filtering presumed nongeophysical velocities in the time series that would be geophysically considered extreme or greater (Worden *et al.*, 2020). Future work should implement more rigorous methods to detect cycle slips in real time to accurately mitigate their impact and a more sophisticated approach to remove nongeophysical signals while preserving the response to extreme events. This approach to detection and removal or repair could be done on the phase measurements directly (de Lacy *et al.*, 2012; Li and Melachroinos, 2019), or potentially identified in least-squares outliers of the phase-derived velocities (Qian *et al.*, 2016; Fratarcangeli *et al.*, 2018). Using a very similar method as employed for the RT-GNSS displacements, the station-dependent velocity noise threshold is set as the 99.5% significance of the NCX2 distribution fit to the quiescent 1 hr time window for each site.

Evaluating events from real-time time series

For this study's evaluation of actual events, hindsight allows us to confidently identify the time-series peaks to test the processing method, not the detection algorithm. This is distinctly different from rapid, real-time detection, in which the peak displacement grows with the evolving, seismic waveforms. To initiate a time window in this study, the Incorporated Research Institutions for Seismology Data Management Center travel-time 1D spherical model web service is used to estimate the *S*- and *P*-wave arrival of a given event at a given station (see Data and Resources). In displacement space, we reference all topocentric displacements relative to the arrival of the *P* wave. PGD always occurs after the *S*-wave arrival, the amount largely dependent on distance but generally tens of seconds behind the *P* wave (Goldberg *et al.*, 2018). Although not exact, the advantage of using this a priori reference versus a fixed one is that it reduces the impact of longer period RT-GNSS PPP drift of stations further from the source. We also window the detection time domain to allow for the full PGD temporal evolution to occur, while also limiting the likelihood of inverting spurious noise. In addition, we also estimate the noise threshold of the 2 min prior to the earthquake origin time using the NCX2 approach and use this as a station- and time-dependent integrity validation: if the peak is not above this noise threshold, the peak does not contribute to the evolving event magnitude estimate. Finally, we filter any nonphysical outliers that are a result of the processing (such as cycle slips), using a coarse threshold of 2 m in displacement space and 1 m/s in velocity space. This limits the impact of potential nongeophysical signals affecting magnitude estimates outside the range of any feasible geophysical signals.

Results

We compare ambient TDCP velocity noise with ambient PPP displacement noise across the same stations over the identical time window to ensure that any potential uncorrected temporal, spatial, or receiver noise dependency is consistent across both the processing methods. We bin each station's threshold for both the velocity and displacement into quartiles of the entire network. In Figure 4, a map is presented in which each station is colored by these quartile estimates. Most notable are the Q4 (red) stations, which have the highest threshold magnitudes and therefore are considered the noisiest. We observe a general correlation between GD and GV, which is logical, given they share many environmental noise factors. We observe

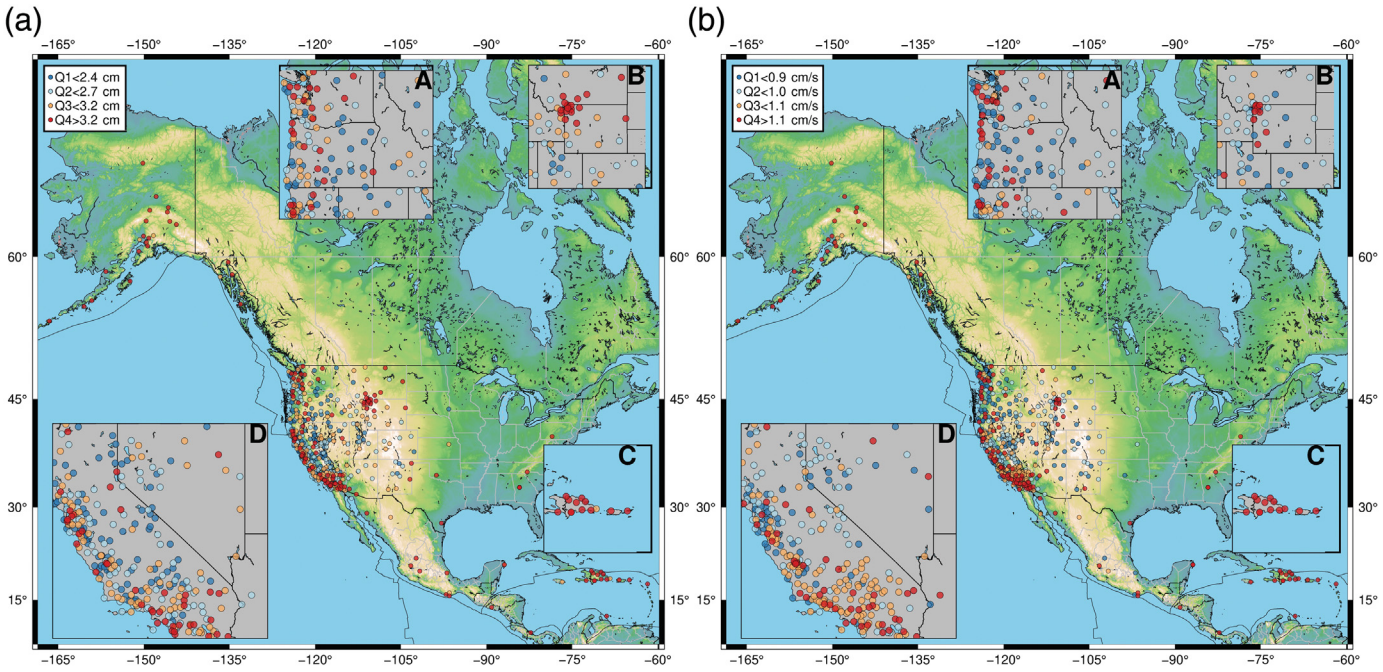

Figure 4. (a) Spatial distribution of position displacement noise estimated from PPP-derived ground displacement and (b) velocity noise estimated for TDCP-derived ground velocity. Inset A is the Pacific Northwest of the United States, inset B is Yellowstone National Park and vicinity, inset C is Hispaniola and vicinity, and inset D is Southern California. The estimated thresholds of each station are binned by quartile of the entire network distribution of thresholds by method. These quartiles are represented by the blue, Q1 markers (the lowest noise) to the red Q4 markers (the highest noise). We observe higher noise (red) regional clusters such as in Yellowstone National Park, Hispaniola, and the Pacific Coastline of the United States. For absolute values, quantitative threshold ranges are included in the legend.

regional clusters of lower performing (red) stations, such as those in the Caribbean, Yellowstone National Park, the Pacific Northwest, and southern California. The southern California and Pacific Northwest areas (insets A and D) have higher station density, so this is not only partially a visual effect from map layering Q4 last, but could also be near-coastal effects such as unmodeled tropospheric gradients. Yellowstone (inset B) has a high density of stations that are in a suboptimal environment in terms of obscured satellite sky-view and vegetation multipath, which likely leads to noisier high-rate position and velocity estimates. The Hispaniola and vicinity sector (inset c) likely also experiences complex tropospheric gradients in the signal paths, in addition to multiple antennas situated by necessity in suboptimal radio frequency environments such as on roofs with higher multipath or partially obscured satellite visibility.

Two other parameters that we assess related to noise thresholds are GNSS receiver type and monument type at a given station. Monumentation effects do not appear to be clearly correlated to noise performance in Figure 5. Much research has been put into evaluating secular velocity noise deriving from monumentation type, but we infer that at these higher frequencies monument stability plays less of a role in ambient noise estimates. Certainly, monumentation plays a role in dynamic station-dependent responses, such as ringing or amplification of surface waves (Hodgkinson *et al.*, 2020) from monumentation instability. A receiver-type comparison offers an interestingly salient correlation: PPP noise estimates do not differ by receiver type, whereas velocity threshold estimates do. We acknowledge the potential that additional interdependence on antenna type or receiver environment might influence this result but infer that this receiver correlation result is predominantly related to the respective processing methods: TDCP-GV derives directly from the receiver-independent broadcast ephemeris and receiver-dependent carrier phase observations. Receiver-dependent carrier phase effects such as receiver-dependent multipath or radio frequency interference mitigation, and oscillator drift rate not accounted for in local oscillator drift estimates impact these TDCP velocity estimates. PPP-GD is derived from the PPP estimates, which are stateful estimates of which the noise is largely driven by the modeled common-mode effects such as the commercial satellite orbits, clocks, and atmospheric products. Possible TDCP receiver-dependent dynamic response performance is not evaluated here.

We take the median of these 592-station noise estimates to represent the ambient noise level of the respective methods; a signal larger than this threshold is considered detectable. Given the scaling laws of Melgar *et al.* (2015) and Fang *et al.* (2020) as our signal model, the noise threshold is used to estimate the detection sensitivity of each method across a range of magnitudes and hypocentral distances. It is worth noting that

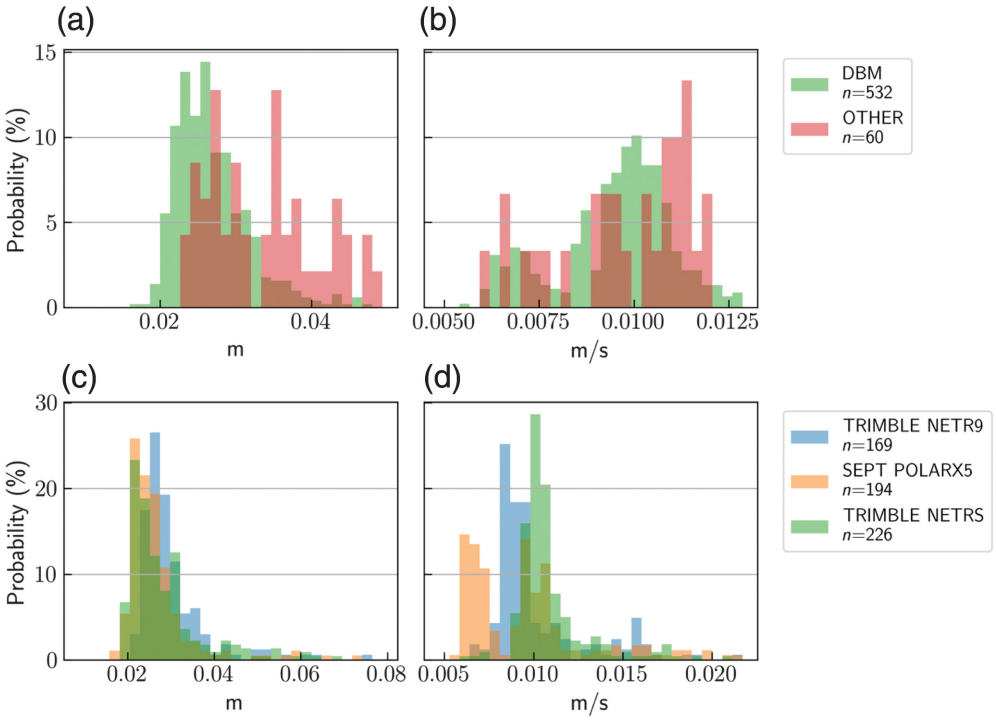

Figure 5. Distributions of noise threshold estimates for the experiment set by antenna monument type (panels a,b) and by receiver type (panels c,d). Panels (a) and (c) are displacement-derived noise thresholds; panels (b) and (d) are velocity-derived noise thresholds. The drill braced monuments include deep and short drill monuments, which are generally stainless steel rods drilled 2–10 m in 3–4 azimuthal directions coupled to a vertical rod just below the antenna mount. "Other" consists of all other monument types, including masts, wellheads, roof mounts, and pillars. The receivers included in the study are Trimble NetR9s, Septentrio PolaRx5s, and Trimble NetRSs. (Note: NetRS solutions are Global Positioning System [GPS]-only; Trimble NetR9s and Septentrio PolaRx5s RTX PPP estimates use GPS and GLONASS.)

we take the network median to compare methods across a large sample set, flattening detection to a binary result. This time-domain station or time-dependent thresholds, however, can also be compared for assessment or potentially real-time integrity monitoring, like the proposed approach of Melgar *et al.* (2020) in the frequency domain; please refer to Figure 3 for a more probabilistic assessment of these sensitivities. In Figure 6, we observe across a range of distances from 5 to 1000 km a lower magnitude sensitivity threshold for the TDCP-PGV relative to PPP-PGD method, given the respective TDCP-PGV and PPP-PGD average noise estimates. We also observe a higher variance in the GV noise estimates that leads to a more distributed station-dependent noise threshold. This aligns with the reported standard errors of the scaling law magnitude uncertainties: 0.27 magnitude units for Melgar *et al.* (2015) PGD method, and 0.389 magnitude units for Fang *et al.* (2020). Figure 6 presents an additional feature to the detection threshold comparison: although the PGV method outperforms with respect to the lower magnitude noise detection threshold, as events get larger in magnitude, the signal of PGD gains magnitude at a greater rate than PGV relative to the static ambient noise, as evident in the nearly converging distal arcs. Given these results, for a given magnitude and distance window, we infer this would lead to the TDCP-PGV method detecting an event by more stations although with greater uncertainty.

Comparison of PPP-PGD versus TDCP-PGV in actual events

We use two well-recorded events as examples of the response of these methods in supporting event detection and real-time magnitude estimates. The GNSS PPP-PGD network response in the 2019 M_w 7.1 Ridgecrest was nominal and is well documented (Hodgkinson *et al.*, 2020; Mattioli *et al.*, 2020; Melbourne *et al.*, 2020; Melgar *et al.*, 2020). The real-time GNSS network density surrounding this event enables a direct comparison of the PPP-PGD and TDCP-PGV methods. In this analysis, 250 sites are used within 375 km to contribute to the PGV and PGD estimates (Fig. 7). Consistent with the previously published studies cited previously, PPP-PGD is within M_w ±0.2 of the final ANSS Comprehensive Earthquake Catalog (ComCat) magnitude of 7.1 in under 20 s. Network latency of position availability is not accounted for in these estimates, though typically these are around 1–2 s (Mattioli *et al.*, 2020).

In this larger magnitude event with many near-field stations, detection sensitivity does not play a noticeable role in rapid magnitude estimation with the majority of waveform magnitudes well above the noise thresholds on arrival at the stations. In Figure 7, the running median estimate by each processing method is depicted by the continuous orange or blue lines; the black dashed line represents the estimates if no thresholding was implemented, which is barely visible due to its minor variance from the thresholded estimate. The increased uncertainties of the PGV estimates though impact the accuracy of the magnitude estimate, evident in the larger spread of the individual station velocity-derived estimates. This result is consistent with the variance of the station-dependent ambient noise thresholds from Figure 6. Except for the initial PGV estimate, both methods initially underestimate the

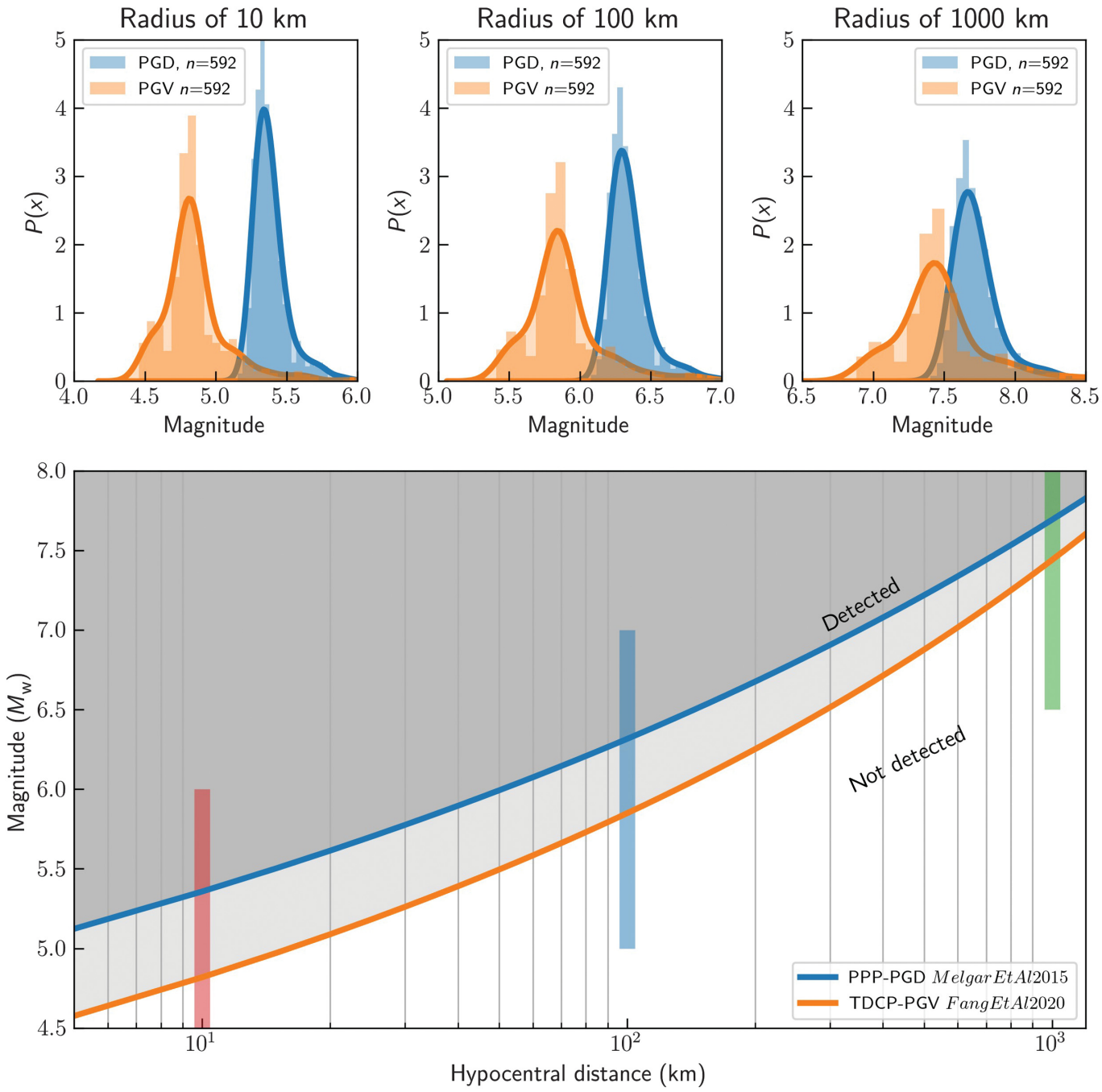

Figure 6. Detection thresholds of each method as a function of hypocentral distance from a given magnitude event. The scaling coefficients used are noted in the legend. The top panels correspond to the color-coded vertical bars in the lower panel. These bars are slices at different hypocentral distances that illustrate the distribution of ambient noise threshold estimates across the 592 stations in the set.

magnitude before converging almost exactly on the final ComCat magnitude of 7.1. This response might be explained by the limitations of existing scaling laws in the near field, treating the events as a simple point source (Goldberg *et al.*, 2021). Within 25 s, both the methods processed independently reach an estimate within ±0.2 magnitude units of the ComCat value to provide useful information in a hazard alert system. Combining or considering both the independent estimates would not address the variance in observed peak deformation from the current point source, isotropic attenuation empirical model, but would add redundancy to the respective estimation processes.

For the M_w 5.3 event, two sites are presented within 12 km hypocentral distance (Fig. 8). We present this smaller set as evidence of the characteristics of the ambient noise model assessed previously: Figures 8f and 8h illustrate the two nearest

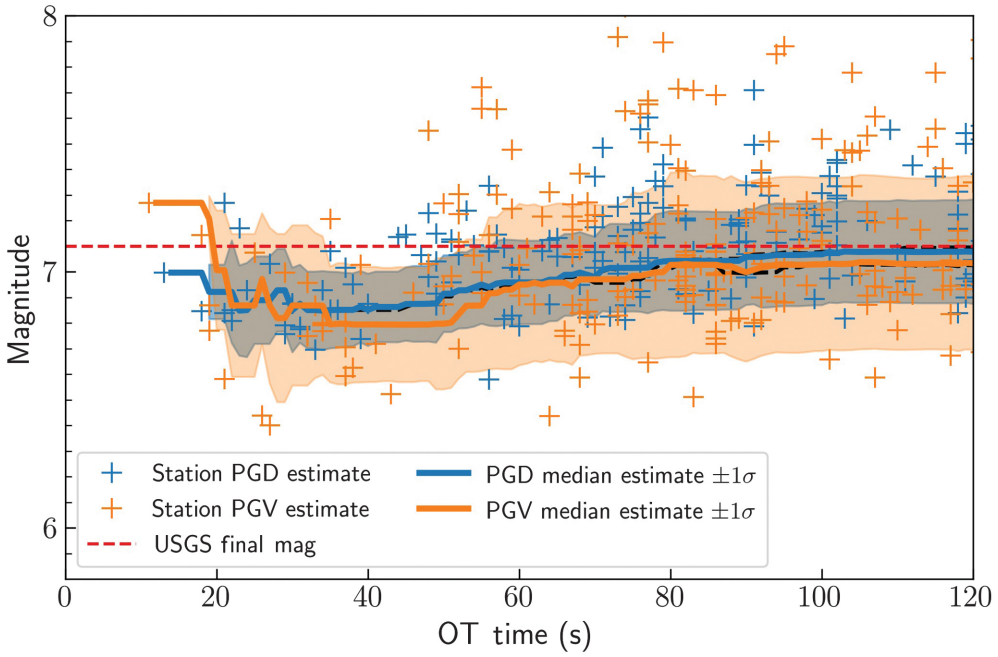

Figure 7. Magnitude estimation evolution over time for the 2019 M_w 7.1 Ridgecrest sequence given individual stations TDCP-PGV and PPP-PGD magnitude estimates. The points represent the individual station magnitude estimates, and the solid lines are the running median event estimate given the available estimates at the time. The stations that are above the noise estimate using the running previous 2 min window are included in this median. The shading represents one standard deviation of the estimates contributing to the magnitude at each epoch. The barely visible black dashed lines are the estimates if no thresholding takes place; this is added to demonstrate that thresholding has little apparent effect in the relative near field of larger events. In this figure, all station's contributions to the overall magnitude estimate are evenly weighted over time. The U.S. Geological Survey Comprehensive Earthquake Catalog final magnitude is the dashed red line.

(<=12 km) receivers detect the M_w 5.3 event in TDCP velocity space, given the aforementioned magnitude threshold. Only the nearest station detects the event above the estimated threshold in PPP displacements. This event is close to the boundary threshold of detection for PPP 3D displacement method, given these individual station noise thresholds. Peak velocity and displacement signals estimate the magnitude within M_w ±0.2 of the final ComCat magnitude 5 s after the origin time. Further visual inspection of Figure 8a,c,e,g's time series of directional components indicates a clear signal in the velocities and a more subtle signal in the displacements. The largely horizontal nature of this event makes the peak magnitude partially obscured by the vertical noise: this is especially true in the second station, P495, velocity time series, where the peak velocity is above the threshold but so are spurious outliers that would lead to greater uncertainty in real-time peak identification. This is also evident in the PPP time series of P507, where a rapid southward motion is evident but ultimately obscured in accumulated noise of the three-component magnitude. The only stations capable of detection are very near the epicenter and thus likely more responsive to near-field source variations, as suggested by Goldberg *et al.* (2018), and yet at this lower end of detectable seismic deformation signals, the scaling velocity relationship passes for these two receivers and for one in displacement space. That the P495 displacement signal fails to go above the threshold yet still estimates the correct magnitude raises some concern about the threshold level if this is indeed a false negative. Future work should further evaluate this balance of false alerts with sensitivity across many events and stations close to the boundary. In summary, these TDCP velocity estimates would offer additional information to detect and characterize coseismic antenna motion in real time that the PPP-derived displacements might not.

Conclusions

For near-field relatively smaller events (M_w ~5–6.5) and/or larger events at greater hypocentral distances, TDCP velocities are more sensitive to detecting seismic surface waves than PPP displacements. PGD grows larger with magnitude relative to PGV; however, thus this advantage of sensitivity falls off with increased magnitude in the relative near field. It is important to note, although the seismic infrastructure signal saturation is not an issue at lower magnitude earthquakes, the TDCP method provides an independent estimate of event detection at that magnitude range. Crowell (2021) emphasizes the role these independent velocity estimates could play in contributing to USGS ShakeMaps of modified Mercalli intensity, a valuable metric for evaluating spatially distributed impacts from coseismic shaking. Future efforts to evaluate lowering this threshold to increase sensitivity without increasing the PFAs could prove useful for incorporating these methods into smaller magnitude detection, complementing existing seismic infrastructure especially in more sparsely instrumented regions. Station-specific TDCP-GV stochastic noise estimates vary more than station-specific PPP-GD noise, which leads to increased variability in estimated sensitivity. This ambient noise difference aligns with historical dynamic signal regressions: current PGD-derived scaling laws have less variance than PGV scaling laws in their log-linear fit and thus are more robust in their magnitude

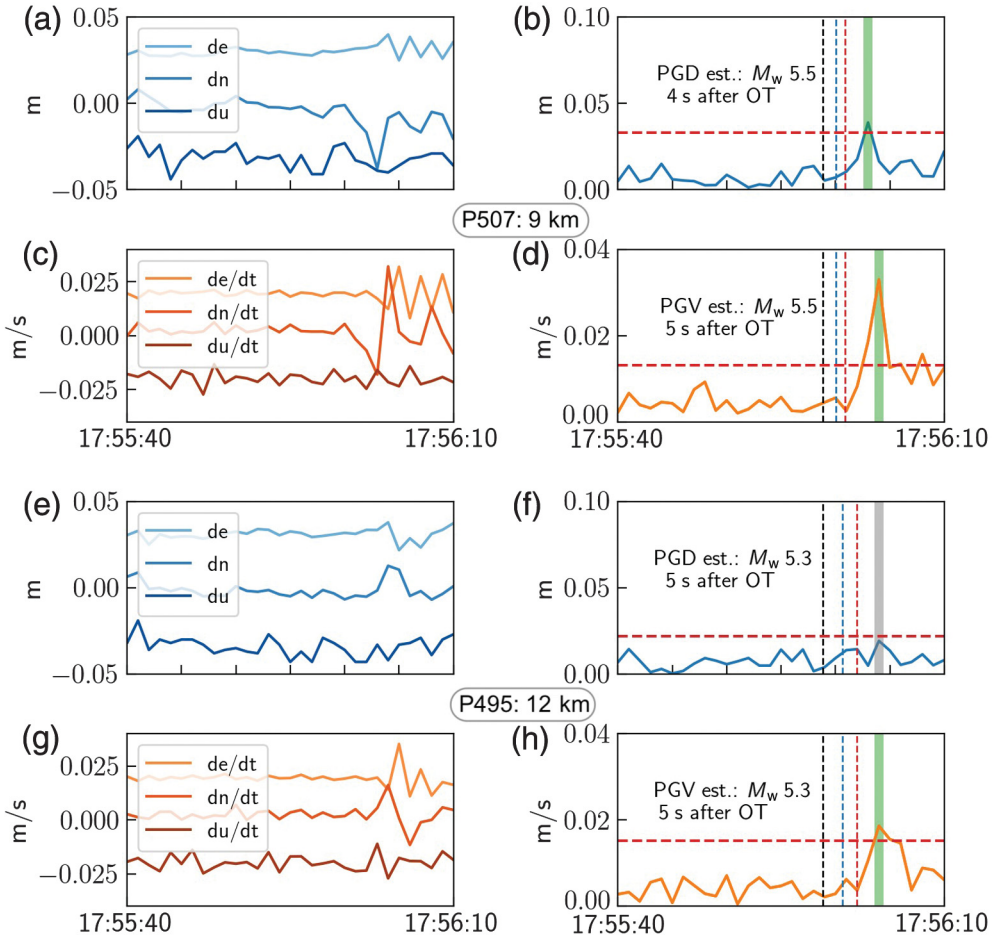

Figure 8. Near-field, two station response in displacement and velocity space for the 2021 M_w 5.3 Calipatria event. Panels (a)–(d) are P507, approximately 9 km hypocentral radius, and panels (e)–(h) are from P495, approximately 12 km hypocentral radius. Each station has four panels: panels (a), (b), (e), and (f) are the time series of vertically offset displacement components (panels a, e) and magnitude (panels b,f), and panels (c), (d), (g), and (h) are vertically offset velocity components (panels c,g) and velocity magnitude (panels d,h), with the running 2 min windowed 99.5% noise estimate prior to the event represented by the horizontal, dashed red line. A green vertical line highlights the peak signal detected by the method in displacement or velocity space that is above the running noise threshold; a gray-vertical line highlights the peak signal detected is below the running noise threshold and thus would not be included in a magnitude estimate. The vertical, dashed black, blue, and red lines are the earthquake origin time, estimated time of arrival of the *P* wave, and estimated arrival of the *S* wave at the station location, respectively. These two stations clearly illustrate the strength of signal relative to the estimated noise in the velocity estimates. This aligns with the modeled signals using the scaling laws from Figure 2.

estimate. Shu *et al.* (2018) demonstrate that aliasing is present in 1 Hz velocity estimates, which would most likely impact the near-field, higher frequency signals. The increased variance in TDCP-PGV is likely related to estimation in velocity space; velocity signal scattering results in a more complex structure (Wu and Zhao, 2006).

TDCP velocities can be computed in real time at the network edge and at higher rates to complement existing PPP displacements and/or traditional seismic methods, including magnitude estimates and Shakemap velocity estimates. This processing method is open source, and free of commercial corrections and proprietary algorithms. Estimating TDCP at higher rates and at the network edge would reduce potential spectral aliasing in lower rate (<=1 Hz) estimates, with substantially less telemetry bandwidth cost compared to centralized processing of higher rate full-fidelity observational streams. The lower cost and increased sensitivity of TDCP velocities, particularly in the near field, makes this method well suited for a potential low cost, dense array experiment to capture and potentially alert for ground motion. The representative noise model of three-component ground-motion (velocity or displacements) magnitudes recommended here can be implemented for a real-time or near real-time temporal and station-dependent characterization. It is important to note that in this analysis we compare two separate processing methods, PPP and TDCP, in two separate detection domains—displacement and velocity. We did this intentionally to assess the respective methods "as is"; however, further work could decouple the processing method from the detection domain.

Data and Resources

Data used in this article are available from the Geodetic Facility for the Advancement of Geoscience (GAGE) Global Navigation Satellite System (GNSS) archives, as maintained by UNAVCO, Inc. The data are available in the raw RINEX (v.2.11) format at ftp://data-out.unavco.org/pub/highrate/1-Hz/rinex/ (Mattioli *et al.*, 2020). The real-time (RT) precise point positioning (PPP) (RTX) solutions are available at ftp://gaia.unavco.org/rtx/. Earthquake depths, locations, and magnitudes came from the Advanced National Seismic System (ANSS) Comprehensive Catalog of Earthquake Events and Products (https://earthquake.usgs.gov/data/comcat/). Arrival times are calculated using the iasp91 velocity model as implemented by Incorporated Research Institutions for Seismology

(IRIS) Web Services (http://service.iris.edu/irisws/traveltime/). Space weather indices are available from GFZ-Potsdam (https://www.gfz-potsdam.de/en/kp-index/) (Matzka *et al.*, 2021). The SNIVEL code package (Crowell, 2021) used to process carrier phase data is available on GitHub at https://github.com/crowellbw/SNIVEL. Maps were made using the Generic Mapping Tools v.6 (Wessel *et al.*, 2019). The SCIPY statistical package is part of the python open-source mathematics library (scipy.org). All websites were last accessed in September 2021.

Declaration of Competing Interests

The authors declare no competing interests.

Acknowledgments

This material is based on services provided by the Geodetic Facility for the Advancement of Geoscience (GAGE) Facility, operated by UNAVCO, Inc., with support from the National Science Foundation (NSF) and the National Aeronautics and Space Administration (NASA) under NSF Cooperative Agreement EAR-1724794. Real-time processing and analysis is supported by NSF OAC-1835791. Upgrades to Network of the Americas (NOTA) real-time stations in California, Oregon, and Washington, D.C., have been funded by the U.S. Geological Survey under ShakeAlert Cooperative Agreements (G17AC00313 and G19AC00287) to UNAVCO, Inc.

References

Allen, R. M., and A. Ziv (2011). Application of real-time GPS to earthquake early warning, *Geophys. Res. Lett.* **38,** L16310.

Bertiger, W., S. D. Desai, B. Haines, N. Harvey, A. W. Moore, S. Owen, and J. P. Weiss (2010). Single receiver phase ambiguity resolution with GPS data, *J. Geod.* **84,** 327–337, doi: 10.1007/s00190-010-0371-9.

Colosimo, G., M. Crespi, and A. Mazzoni (2011). Real-time GPS seismology with a stand-alone receiver: A preliminary feasibility demonstration, *J. Geophys. Res.* **116,** no. B11, doi: 10.1029/2010JB007941.

Crowell, B. W. (2021). Near-field strong ground motions from GPS-derived velocities for 2020 Intermountain Western United States earthquakes, *Seismol. Res. Lett.* doi: 10.1785/0220200325.

Crowell, B. W., D. Melgar, Y. Bock, J. S. Haase, and J. Geng (2013). Earthquake magnitude scaling using seismogeodetic data, *Geophys. Res. Lett.* **40,** 6089–6094, doi: 10.1002/2013GL058391.

de Lacy, M. C., M. Reguzzoni, and F. Sansò (2012). Real-time cycle slip detection in triple-frequency GNSS, *GPS Solut.* **16,** 353–362, doi: 10.1007/s10291-011-0237-5.

Fang, R., J. Zheng, J. Geng, Y. Shu, C. Shi, and J. Liu (2020). Earthquake magnitude scaling using peak ground velocity derived from high-rate GNSS observations, *Seismol. Res. Lett.* **92,** no. 1, 227–237.

Ferrari, A. (2019). A note on sum and difference of correlated chi-squared variables, available at http://arxiv.org/abs/1906.09982 (last accessed November 2021). Preprint posted 24 June 2019.

Fratarcangeli, F., M. Ravanelli, A. Mazzoni, G. Colosimo, E. Benedetti, M. Branzanti, G. Savastano, O. Verkhoglyadova, A. Komjathy, and M. Crespi (2018). The variometric approach to real-time high-frequency geodesy, *Rendiconti Lincei. Scienze Fisiche e Naturali* **29,** 95–108, doi: 10.1007/s12210-018-0708-5.

Genrich, J. F., and Y. Bock (2006). Instantaneous geodetic positioning with 10–50 Hz GPS measurements: Noise characteristics and implications for monitoring networks, *J. Geophys. Res.* **111,** no. B3, doi:10.1029/2005JB003617.

Goldberg, D. E., D. Melgar, Y. Bock, and R. M. Allen (2018). Geodetic observations of weak determinism in rupture evolution of large earthquakes, *J. Geophys. Res.* **123,** 9950–9962, doi: 10.1029/2018JB015962.

Goldberg, D. E., D. Melgar, G. P. Hayes, B. W. Crowell, and V. J. Sahakian (2021). A ground-motion model for GNSS peak ground displacement, *Bull. Seismol. Soc. Am.* doi: 10.1785/0120210042.

Grapenthin, R., M. West, C. Tape, M. Gardine, and J. Freymueller (2018). Single-frequency instantaneous GNSS velocities resolve dynamic ground motion of the 2016 Mw 7.1 Iniskin, Alaska, earthquake, *Seismol. Res. Lett.* **89,** 1040–1048.

Hodgkinson, K. M., D. J. Mencin, K. Feaux, C. Sievers, and G. S. Mattioli (2020). Evaluation of earthquake magnitude estimation and event detection thresholds for real-time GNSS networks: Examples from recent events captured by the network of the Americas, *Seismol. Res. Lett.* **91,** 1628–1645.

Hohensinn, R., and A. Geiger (2018). Stand-alone GNSS sensors as velocity seismometers: Real-time monitoring and earthquake detection, *Sensors* **18,** no. 11, 3712, doi: 10.3390/s18113712.

Larson, K M. (2009). GPS seismology, *J. Geod.* **83,** nos. 3/4, 227–233.

Larson, K. M., P. Bodin, and J. Gomberg (2003). Using 1-Hz GPS data to measure deformations caused by the Denali fault earthquake, *Science* **300,** no. 5624, 1421–1424.

Leandro, R., H. Landau, M. Nitschke, M. Glocker, S. Seeger, X. Chen, A. Deking, M. Ben Tahar, F. Zhang, K. Ferguson, *et al.* (2011). RTX positioning: The next generation of cm-accurate real-time GNSS positioning, *Proc. of the 24th International Technical Meeting of the Satellite Division of The Institute of Navigation (ION GNSS 2011)*, Portland, Oregon, September 2011, 1460–1475.

Li, T., and S. Melachroinos (2019). An enhanced cycle slip repair algorithm for real-time multi-GNSS, multi-frequency data processing, *GPS Solut.* **23,** doi: 10.1007/s10291-018-0792-0.

Mattioli, G. S., D. A. Phillips, K. M. Hodgkinson, C. Walls, D. J. Mencin, B. A. Bartel, D. J. Charlevoix, C. Crosby, M. J. Gottlieb, B. Henderson, *et al.* (2020). The GAGE data and field response to the 2019 Ridgecrest earthquake sequence, *Seismol. Res. Lett.* doi: 10.1785/0220190283.

Matzka, J., C. Stolle, Y. Yamazaki, O. Bronkalla, and A. Morschhauser (2021). The geomagnetic Kp index and derived indices of geomagnetic activity, *Sp. Weather* **19,** no. 5, e2020SW002641.

Melbourne, T. I., W. M. Szeliga, V. Marcelo Santillan, and C. W. Scrivner (2020). 25-second determination of 2019 7.1 Ridgecrest earthquake coseismic deformation, *Bull. Seismol. Soc. Am.* **110,** no. 4, 1680–1687.

Melgar, D., B. W. Crowell, J. Geng, R. M. Allen, Y. Bock, S. Riquelme, E. M. Hill, M. Protti, and A. Ganas (2015). Earthquake magnitude calculation without saturation from the scaling of peak ground displacement, *Geophys. Res. Lett.* **42,** no. 13, 5197–5205, doi: 10.1002/2015GL064278.

Melgar, D., B. W. Crowell, T. I. Melbourne, W. Szeliga, M. Santillan, and C. Scrivner (2020). Noise characteristics of operational real-time high-rate GNSS positions in a large aperture network, *J. Geophys. Res.* **125,** e2019JB019197.

Melgar, D., T. I. Melbourne, B. W. Crowell, J. Geng, W. Szeliga, C. Scrivner, M. Santillan, and D. E. Goldberg (2019). Real-time

high- rate GNSS displacements: Performance demonstration during the 2019 Ridgecrest, California, earthquakes, *Seismol. Res. Lett.* **91,** no. 4, 1943–1951, doi: 10.1785/0220190223.

Minson, S. E., A. S. Baltay, E. S. Cochran, T. C. Hanks, M. T. Page, S. K. McBride, K. R. Milner, and M.-A. Meier (2019). The limits of earthquake early warning accuracy and best alerting strategy, *Sci. Rept.* **9,** doi: 10.1038/s41598-019-39384-y.

Misra, P., and P. Enge (2011). *Global Positioning System: Signals, Measurements and Performance*, Second Ed., Ganga-Jamuna Press, Lincoln, Mass, 569 pp.

Murray, J. R., N. Bartlow, Y. Bock, B. A. Brooks, J. Foster, J. Freymueller, W. C. Hammond, K. Hodgkinson, I. Johanson, A. López-Venegas, *et al.* (2019). Regional global navigation satellite system networks for crustal deformation monitoring, *Seismol. Res. Lett.* **91,** 552–572, doi: 10.1785/0220190113.

Ohta, Y., T. Kobayashi, H. Tsushima, S. Miura, R. Hino, T. Takasu, H. Fujimoto, T. Linuma, K. Tachibana, T. Demachi, *et al.* (2012). Quasi real-time fault model estimation for near-field tsunami forecasting based on RTK-GPS analysis: Application to the 2011 Tohoku-Oki earthquake (Mw 9.0), *J. Geophys. Res.* **117,** no. B2, doi: 10.1029/2011JB008750.

Qian, C., H. Liu, M. Zhang, B. Shu, L. Xu, and R. Zhang (2016). A geometry-based cycle slip detection and repair method with time-differenced carrier phase (TDCP) for a single frequency global position system (GPS) + BeiDou navigation satellite system (BDS) receiver, *Sensors* **16,** no. 12, 2064, doi: 10.3390/s16122064.

Ruhl, C., D. Melgar, J. Geng, D. E. Goldberg, B. W. Crowell, R. M. Allen, Y. Bock, S. Barrientos, S. Riquelme, J. C. Baez, *et al.* (2019). A global database of strong-motion displacement GNSS recordings and an example application to PGD scaling, *Seismol. Res. Lett.* **90,** 271–279, doi: 10.1785/0220180177.

Sheldon James Press (1966). Linear combinations of non-central chi-square variates, *Ann. Math. Statist.* **37,** no. 2, 480–487, JSTOR, available at www.jstor.org/stable/2238621 (last accessed September 2021).

Shu, Y., R. Fang, M. Li, C. Shi, M. Li, and J. Liu (2018). Very high-rate GPS for measuring dynamic seismic displacements without aliasing: Performance evaluation of the variometric approach, *GPS Solut.* **22,** 121, doi: 10.1007/s10291-018-0785-z.

van Graas, F., and A. Soloviev (2004). Precise velocity estimation using a stand-alone GPS receiver, NAVIGATION, *J. Inst. Navigation* 51**,** no. 4, 283–292.

Wessel, P., J. F. Luis, L. Uieda, R. Scharroo, F. Wobbe, W. H. F. Smith, and D. Tian (2019). The generic mapping tools version 6, *Geochem. Geophys. Geosyst.* **20,** 5556–5564, doi: 10.1029/2019GC008515.

Worden, C. B., E. M. Thompson, M. Hearne, and D. J. Wald (2020). ShakeMap Manual Online: Technical manual, user's guide, and software guides, *U.S. Geol. Surv.* doi: 10.5066/F7D21VPQ.

Wu,, Y. M., and L. Zhao (2006). Magnitude estimation using the first three seconds P-wave amplitude in earthquake early warning, *Geophys. Res. Lett.* **33,** L16312.

Zumberge,, J. F., M. B. Heflin, D. C. Jefferson, M. M. Watkins, and F. H. Webb (1997). Precise point positioning for the efficient and robust analysis of GPS data from large networks, *J. Geophys. Res.* **102,** no. B3, 5005–5017, doi: 10.1029/96JB03860.

Manuscript received 20 September 2021
Published online 26 January 2022